Harnessing Multiple Internal Reflections to Design Highly Absorptive Acoustic Metasurfaces

Chen Shen[*] and Steven A. Cummer[†]

*Department of Electrical and Computer Engineering, Duke University,
Durham, North Carolina 27708, USA*

The rapid development of metasurfaces has enabled numerous intriguing applications with acoustically thin sheets. Here we report the theory and experimental realization of a nonresonant sound-absorbing strategy using metasurfaces by harnessing multiple internal reflections. We theoretically and numerically show that the higher-order diffraction of thin gradient-index metasurfaces is tied to multiple internal reflections inside the unit cells. Highly absorbing acoustic metasurfaces can be realized by enforcing multiple internal reflections together with a small amount of loss. A reflective gradient-index acoustic metasurface is designed based on the theory, and we further experimentally verify the performance using a three-dimensional printed prototype. Measurements show over 99% energy absorption at the peak frequency and a 95% energy absorption bandwidth of around 600 Hz. The proposed mechanism provides an alternative route for sound absorption without the necessity of high absorption of the individual unit cells.

DOI: 10.1103/PhysRevApplied.9.054009

I. INTRODUCTION

Sound mitigation and noise reduction have long been active research areas in the field of acoustics because of their usefulness in everyday life [1,2]. Conventional passive sound-absorbing strategies require porous materials or resonant structures to achieve high absorption. While sound-absorbing materials exhibit a strong absorption coefficient at certain frequencies, their ability to absorb sound waves relies on their intrinsic physical properties, which are difficult to be engineered to meet specific requirements. Besides, it may be inconvenient to use a porous medium at low frequencies, since its thickness should be comparable to the wavelength of incoming acoustic waves. Engineered sound-absorbing structures, on the other hand, can be a good candidate for noise reduction, as their performance can be tailored to operate at target frequencies. However, traditional sound-absorbing structures such as perforated panels [3] are usually bulky, as the thickness of the back cavity cannot be deeply subwavelength, and their bandwidth is typically narrow for resonance-based structures. Active absorbers, while showing great potential on tunability and flexibility especially at low frequencies, require sophisticated electrical circuits, which inevitably add system complexity and fabrication challenges [4–6].

The recent emergence of acoustic metamaterials and metasurfaces has diversified the functionalities of sound manipulation and provides an efficient means for designing novel sound-absorbing structures [7–9]. Various resonant structures are reported for sound mitigation. For example, coupled Helmholtz resonators [10,11], coplanar chambers [12,13], labyrinthine metamaterials [14–16], gas inclusions [17], and membrane resonators [18,19] are proposed to achieve high energy absorption at desired frequencies with a subwavelength thickness. However, since these metasurface-based absorbers are based on local structural resonances (i.e., the acoustic energy is converted to other forms of energy near the resonance frequency), they are typically associated with inherently constrained limited bandwidth or poor uniformity. Moreover, their macroscopic performance relies strongly on the individual response of the unit cells within the structure. For instance, porous or fibrous materials like sponge and cotton are used in labyrinthine metamaterials to tailor their acoustical behavior for better performance for higher absorption [15,16]. These requirements make them inconvenient for integration into larger scales and inevitably hinder their real-world applications.

A nonresonant metasurface, on the other hand, can potentially have a wider bandwidth and better uniformity. More importantly, the acoustic response of individual unit cells does not need to be tuned to induce local resonance. Such metasurfaces are thus highly desired in the acoustic community for practical applications in various scenarios provided that the internal physics can be controlled to maximize absorption in a relatively thin structure. Recently, a sound-absorbing mechanism based on multiple internal reflections (MIR) is proposed within the context of gradient-index metasurfaces (GIMs) [20,21]. The effect of MIR which is critical for the explanation of diffraction,

[*]chen.shen4@duke.edu
[†]cummer@duke.edu

however, is not discussed, and no explicit details are given on the design of an absorptive metasurface by maximizing the effect of MIR.

In this paper, we fully analyze the diffraction of GIMs and reveal the dominant role of MIR in the unit cells. We show that, by specifically engineering the phase gradient of the metasurface, high acoustic absorption can be achieved in a nonresonant manner. The phenomenon is realized by tailoring the MIR process which effectively increases the time for acoustic waves trapped inside the metasurface before exiting. The importance of MIR in controlling acoustic-wave behaviors in GIMs is manifested using an absorptive metasurface. Notably, the metasurface is realized with a finite thickness to increase the time interaction with the acoustic waves. The thickness, on the other hand, can be less than half of the wavelength (0.4λ in this study), which is thin enough to be characterized as a "metasurface." Analytical calculations based on the coupled-mode theory are used to predict the behavior of the metasurface, and it is further verified by numerical simulations with a finite-element analysis. Measurements of a three-dimensional (3D) printed prototype are further performed to validate our design strategy. The mechanism proposed in this paper may pave the way for sound-absorbing structures without a dependence of local resonance.

II. THEORY

A. Coupled-mode theory

To illustrate the concept, we first consider a GIM shown in Fig. 1. The GIM is backed with a rigid wall and functions as a reflective metasurface. Without the loss of generality, the metasurface consists of N unit cells per period and extends in the x direction. Each unit cell has a width d and thickness h, and the periodicity of the GIM is $\Gamma = Nd$. The whole system is immersed in a background medium (air in this study) with density $\rho_0 = 1.2$ kg/m³ and speed of sound $c_0 = 343$ m/s. The incident is a plane wave given by

$$p_i(x, y) = p_0 e^{ik_x x} e^{-ik_y y}, \qquad (1)$$

where p_0 is the amplitude of the incident wave, $k_x = k_0 \sin\theta_i$ and $k_y = k_0 \cos\theta_i$ are the wave numbers with θ_i
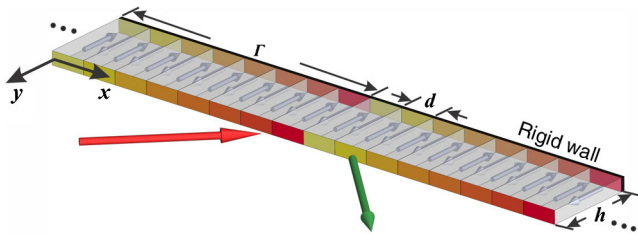

FIG. 1. Schematic diagram of a reflective GIM. The red and green arrows represent incident and scattered waves, respectively. The white arrows inside the GIM illustrates the MIR process.

being the incident angle, $k_0 = (2\pi/\lambda)$ is the free space wave vector, and λ is the wavelength of the incident wave.

Using the coupled-mode theory [21–23], the scattered field can be expressed as a summation of different diffraction orders given by Floquet harmonics:

$$p_r(x, y) = \sum_m r_m e^{ik_{y,m} y} e^{ik_{x,m} x}, \qquad (2)$$

where $k_{y,m} = \sqrt{k_0^2 - k_{x,m}^2}$ is the y-component wave vector with $k_{x,m} = k_x + m(2\pi/\Gamma)$ being the transverse-wave component and r_m is the normalized reflection coefficient associated with the mth diffractive order. Since the width of the unit cells is deeply subwavelength (i.e., $d \ll \lambda$), they can be regarded as thin slits as they are separated by rigid walls, and only the fundamental mode can be supported inside the slits. The pressure field inside the metasurface can thus be expressed as

$$p_{\mathrm{ms}}(x, y) = a_i e^{ik_i y} + b_i e^{-ik_i(y+h)}. \qquad (3)$$

The subscript ms denotes the metasurface, a_i and b_i are the coefficients of the forward and backward waves, respectively, $k_i = n_i k_0$ is the wave vector in the ith slit, and n_i is the corresponding refractive index. Since the acoustic pressure is zero at $y = -h$ because of the hard boundary, b_i is given by

$$b_i = -a_i e^{-ik_i h}. \qquad (4)$$

By enforcing the continuity of pressure and vertical velocity at $y = 0$, we obtain

$$\sum_m \left(\delta_{0,m} + r_m\right) e^{ik_{x,m}\alpha_i} g_m = a_i + b_i \phi_i, \qquad (5)$$

$$\frac{\left(k_{y,m}\delta_{0,m} + r_m k_{y,m}\right)\Gamma}{\rho_0} = \sum_{i=1}^N \frac{k_i d\left(a_i - b_i \phi_i\right) e^{-ik_{x,m}\alpha_i}}{\rho_i} g_m, \qquad (6)$$

where $\delta_{0,m}$ is the Kronecker delta, $\alpha_i = id - (d/2)$ and $\rho_i = n_i \rho_0$ are the position and effective density, respectively, of the ith unit cell with n_i being the effective index, $\phi_i = e^{-ik_i h}$ is the phase change across each unit cell, and $g_m = \mathrm{sinc}(k_{x,m} d/2)$. By solving Eqs. (4)–(6), the reflection coefficient associated with each diffractive order can be solved.

We begin with a reflective GIM composed of 12 unit cells; the width d and thickness h are 2.5 and 4 cm, respectively, and the frequency of the incident wave is 3100 Hz. Note that the phase gradient along the metasurface $\xi_1 = (\partial\phi/\partial x) = (2\pi/\Gamma)$ is equal to the diffraction caused by periodicity; the fundamental mode scattering
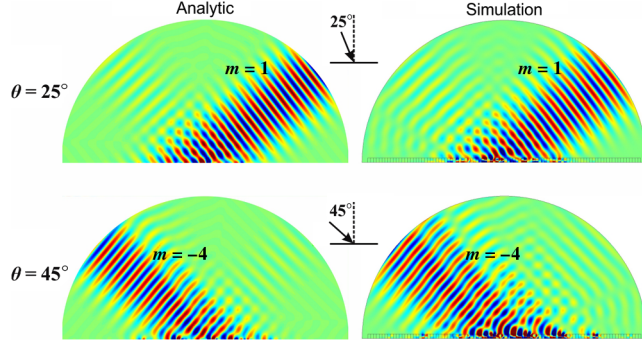
FIG. 2. Scattered acoustic field from a reflective GIM. Left: Analytic field. Right: Simulated field. The incident wave is omitted for better visualization. Higher orders of diffraction are observed when the incident angle is above the critical angle.

(i.e., $m = 1$) can thus be interpreted as a metasurface dictated by the generalized Snell law [24]. The critical angle for fundamental mode scattering can be easily obtained as $\theta_c = \sin^{-1}(1 - \xi_1/k_0) = 39.1°$. Two cases are analyzed, namely, $\theta_1 = 25°$ and $\theta_2 = 45°$. In the first case, the incidence angle is below the critical angle, and the fundamental mode dominates. In the second case, a higher-order mode ($m = -4$) dominates, because the fundamental mode becomes evanescent as $k_{x,1} > k_0$. The acoustic field is also calculated from numerical simulations based on COMSOL Multiphysics for comparison. The corresponding scattered acoustic fields are plotted in Fig. 2, with excellent agreement between the analytic results and numerical simulations. The small discrepancies in the near field may be caused by the radiation patterns of the individual cells, which is not accounted for in the theory. The amplitude and direction of each diffraction mode are well captured by the analytic model, proving the validity of the theoretical approach.

B. Multiple internal reflections in the unit cells

Interestingly, it can be seen from Fig. 2 that, when the incident angle is above the critical angle, negative refraction is induced and there is a sudden jump of the diffraction order from $m = 1$ to $m = -4$. Note that the propagation mode is allowed when $k_{x,m} < k_0$; while multiple diffraction modes ($m = -4–0$) satisfy the relation, $m = -4$ dominates, and other modes are hardly visible in Fig. 2. This abrupt change of the diffraction order has been reported previously [20,21,25], but the physical mechanism of this phenomenon and how the diffracted waves are formed have yet to be fully studied.

We now begin with the analysis based on MIR. This will reveal the formation of each diffraction order and explain the reason for the abrupt mode change above the critical angle. Recall that, for the GIM under study, each period contains 12 individual unit cells. As the phase change within a period

covers a complete 2π for a reflective GIM, the relative local phase accumulations (i.e., the exiting phase compared with the incoming phase) across each unit cell when the acoustic waves are directly reflected from the rigid backing are $(\pi/6), (2\pi/6), (3\pi/6), …, (10\pi/6), (11\pi/6), (12\pi/6)$, respectively. In other words, for an incoming wave with wave vector k_x, the reflection inside the slits will induce an extra momentum in the x direction, which is the same with the phase gradient ξ_1 of the GIM. The outgoing wave will therefore exhibit an x component wave vector of $k_x + \xi_1$. By noting that $k_{x,m} = k_x + m(2\pi/\Gamma)$, it can be concluded that one reflection inside the unit cells corresponds to the case of $m = 1$, which is also the scenario dictated by the generalized Snell law. Similarly, for a MIR process of two-times reflection inside the unit cells (i.e., the acoustic waves reflect twice at the boundaries at $y = -h$), the relative phase change across the cells becomes $(\pi/3), (2\pi/3), (3\pi/3), …, (10\pi/3), (11\pi/3), (12\pi/3)$. The extra parallel momentum is $\xi_2 = (\partial\phi/\partial x) = (4\pi/\Gamma)$; by adding this momentum to k_x, the outgoing wave vector can be obtained as $k_{x,2} = k_x + \xi_2$, which corresponds to a diffractive order of $m = 2$. Likewise, diffraction with the order of $m > 0$ is formed as the waves are multiply reflected m times inside the slits.

For diffractive orders taking negative values or zero, i.e., $m \le 0$, the occurrence of MIR can be predicted based on the fact that a phase wrap of 2π is equivalent to 0. For example, for the local phase accumulations of one-time reflection, a phase difference of -2π can be enforced such that the phase gradient becomes $(\partial\phi/\partial x) = -(22\pi/\Gamma)$, with the phase difference between adjacent unit cells interpreted as $-\frac{11}{6}\pi$ rather than $\frac{1}{6}\pi$. The diffractive order m with this phase gradient is therefore $-(22\pi/\Gamma)/\xi_1 = -11$. This indicates that, for a direct reflection, the diffraction order can be regarded as either $m = 1$ or, equivalently, $m = 1 - N$, depending on the incident wave vector ($|k_x + \xi| < k_0$ for the propagating mode). Similarly, a diffraction order of m (m is positive and $m < N$) is also equivalent to $m - N$, since they share the same number of multiple reflections. Since N reflections represent a phase wrap of 2π, any MIR greater than N times can be neglected, as they can be reduced to $N - 12n$ ($n \in Z$). For the case shown in Fig. 2 for $\theta_2 = 45°$, although multiple diffraction orders ($m = -4, -3, -2, -1, 0$) can exist for a propagating wave, the number of times needed for MIR, however, is different. From the above analysis, for nonpositive m, the corresponding occurrence of MIR is $m + N$. This indicates that a negative m with a greater absolute value corresponds to fewer multiple reflections, for which acoustic waves will be less retarded inside the metasurface and, hence, greater dominance. For example, eight reflections are needed to generate the $m = -4$ mode, while for $m = 0$, 12 times of MIR must occur. This explains that, for incident angles above the critical angle, the diffractive order always jumps to the smallest negative value that is allowed, as that value takes the least time of MIR for the formation of a propagating
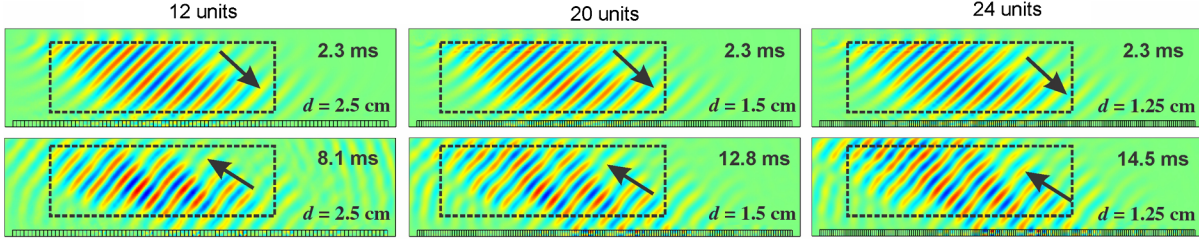
FIG. 3.   Transient simulations for GIMs with different resolutions. The left, middle, and right panels represent GIMs with 12, 20, and 24 unit cells within one period, respectively. The dotted black boxes mark the incident and diffracted beams, and the time when a snapshot of the fields is taken is given by the time in the individual panels. Top: The incident field indicating the GIMs are illuminated at the same time. Bottom: The formation of a similar scattered field pattern for $m = -4$ diffraction order, indicating a different MIR process occurs within each GIM.

wave. This diffraction order can be calculated by solving the smallest possible propagating mode:

$$m = \text{roundup}\left(-\frac{2k_0}{\xi_1}\right) + 1. \qquad (7)$$

Another quite interesting conclusion based on the MIR analysis is that the occurrence of MIR $(m + N)$ is dependent on the number of unit cells per period when m is nonpositive. This indicates that the occurrence of MIR can be increased by discretizing the metasurface with more unit cells within one period without changing the phase gradient. In other words, a more finely resolved GIM would result in more multiple reflections inside the slits and more net time delay within the metasurface. To confirm this phenomenon, transient numerical simulations are conducted. Three reflective GIMs with the same phase gradient but different resolutions are constructed, each containing 12, 20, and 24 unit cells per period, respectively. The unit cells are characterized by an impedance-matched effective medium with varying refractive indices. At $t = 0$ ms, a spatially modulated Gaussian beam is generated with an incident angle of 45° on the metasurface, which is greater than the critical angle. The duration of the incident signal is 2 ms, and the time is recorded when the $m = -4$ diffracted wave is fully formed; the results are shown in Fig. 3. It can be seen that more time is needed for the formation of the diffracted beam by increasing the number of unit cells in the GIMs. This is consistent with the analysis, as more MIR takes place inside the metasurface of a higher resolution.

Since more delay within the metasurface will result in a higher absorption when loss is introduced [21], the MIR process is further verified by introducing loss in the metasurface. We first consider the case for a loss factor of $\gamma = 0.01$. The loss is modeled simply as an imaginary part of the wave vector inside the unit cells, i.e., $k_i = n_i k_0 (1 + \gamma i)$. Figure 4(a) shows the scattered acoustic fields from the two GIMs when loss is considered. The MIR is enforced, and $m = -4$ order dominates the scattered field as expected. It is found that the amplitude for this diffraction order in the two GIMs is different, which is in good agreement with the MIR analysis. Remarkably, a finer resolution of the GIMs (24 units) yields a higher absorption
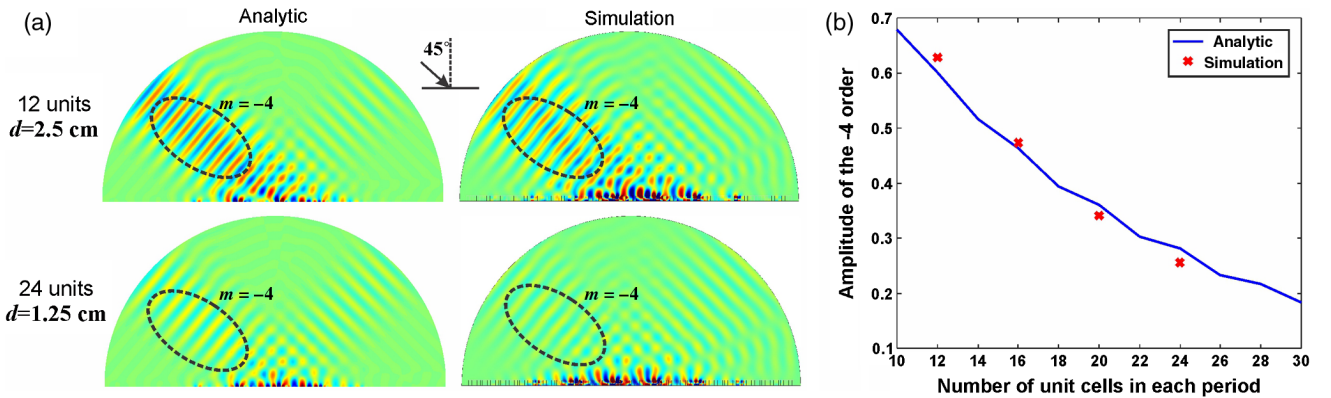

FIG. 4.   (a) Scattered acoustic field from three reflective GIMs with different resolutions. Top: GIM with 12 unit cells per period with a width of 2.5 cm. Bottom: GIM with 24 unit cells per period with a width of 1.25 cm. The left and right panels depict the analytic field and simulated field, respectively. The scattered wave with a diffraction order of $m = -4$ is marked with the dotted box. The incident wave is omitted for better visualization. (b) Analytically and numerically calculated $m = -4$ order amplitude. The amplitude decreases with more unit cells in each period, showing that the amplitude of higher-order diffraction is dependent on the resolution of the metasurface.

coefficient; this is because, by discretizing the metasurface into more unit cells, more occurrences of MIR are enforced and a longer time is spent for acoustic waves before leaving the metasurface. In this way, a higher absorption is achieved without increasing the loss factor of the individual cells. This is further proved by calculating the amplitude of the $m = -4$ order diffraction by gradually changing the resolution of the GIMs while keeping the same loss factor of the unit cells, as depicted in Fig. 4(b). It should also be pointed out that, since the theory and simulation presented here assume an effective medium with matched impedance, it confirms that the strategy is different from previous absorptive metasurfaces which involve local resonances.

III. DESIGNING AN ABSORBING METASURFACE BASED ON MULTIPLE INTERNAL REFLECTIONS

A. Design

The theory outlined in Sec. II provides the understanding and insight to enable the design of a highly absorptive metasurface by harnessing the MIR process. Since MIR dominates above the critical angle (otherwise, the acoustic wave will induce a direct reflection $m = 1$, which is the generalized Snell law), the GIM will work as an absorber only for incidence angles for which the $m = 1$ diffractive order is nonpropagating. This is easiest for larger angles of incidence but can be circumvented by increasing the spatial phase gradient of the GIM. Note that the scattered waves obey the wave vector relation $k_{x,m} = k_x + m\xi_1$, and the condition $|k_{x,m}| \leq k_0$ allows a propagating $m = 1$ diffractive order. For a large phase gradient, e.g., $\xi_1 > 2k_0$, only $m = 0$ supports a radiating diffraction [23]. All other modes result in $|k_{x,m}| > k_0$, which represents nonradiating surface waves. Since N times of MIR is needed to excite the $m = 0$ mode, this means that, for an incoming wave with arbitrary direction, MIR will be induced before the propagating waves leave the metasurface. The outgoing transverse wave vector will be the same with the incident one as

$k_{x,0} = k_x$. A metasurface absorber can thus be achieved by further introducing a suitable amount of loss in the unit cells.

We begin with a reflective GIM operating at 3100 Hz. The width a unit cell is chosen to be 7 mm in order to yield a fine resolution of the GIM, and each period contains eight unit cells. The periodicity Γ is therefore 5.6 cm, which is close to the theoretical limit of 5.53 cm to satisfy $\xi_1 > 2k_0$. A hybrid structure consisting of shunted Helmholtz resonators and a straight channel is used to control the local phase shift in a piecewise manner. Other structures that can modulate the reflective phase with appropriate inherent loss can also work, in principle, such as space-coiling metamaterials [26], spiral cells [25], helical structures [27], and so on. We choose the hybrid structure, as it features a thin width for finer resolution to induce more MIR inside the metasurface. The operation frequency is chosen to ensure a 2π phase span for the given size of the unit cells, and the geometry can be tuned to realize functionality at other frequencies. Similar structures are reported to control the transmitted phase [21,28,29], and they are modified here for the sake of reflective phase control. The height of the Helmholtz resonators is adjusted to tune the reflected phase, and the operation frequency is far below the resonance frequencies of the Helmholtz resonators. The geometry and reflected pressure fields of the unit cells without loss are illustrated in Figs. 5(a) and 5(b), where a linear phase change between adjacent unit cells can be observed. The thickness of the unit cells is 46 mm and is less than half of the working wavelength. These unit cells ensure accurate phase modulation, and the neck of the Helmholtz resonators and thin straight channels can introduce thermoviscous dissipation that is required for sound absorption [21,30]. Although viscous and thermal losses are proposed to obtain quasiperfect sound absorption near resonance [31–33], the mechanism proposed here is totally different, since resonance is not mandatory and the metasurface is not operating near the resonance of the individual unit cells. Moreover, only a small loss factor is needed for satisfactory high absorption. The loss factor of the unit cells
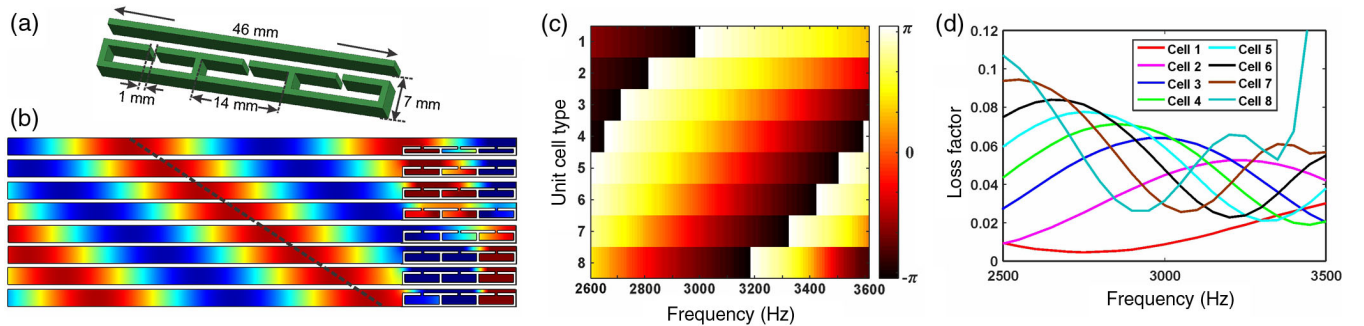

FIG. 5.   Design of the absorptive metasurface. (a) Geometry of a unit cell. (b) Simulated reflected acoustic fields for different unit cells by increasing the height of the Helmholtz resonators. The dotted line denotes an equiphase contour which shows an equal phase shift of $\pi/4$ between adjacent unit cells. (c) Retrieved loss factors of the unit cells. At the designed frequency (3100 Hz), the average loss factor is 0.043. (d) Reflected phase map of the unit cells.

is estimated numerically using the thermoviscous acoustics module in COMSOL. The absorption caused by thermal and viscous dissipation is compared with an effective medium with identical sizes of the real structure. The loss factor of the unit cells can be obtained by choosing a suitable loss factor γ in the effective medium such that the absorption in the two models is equal [21]. Figure 5(c) shows the retrieved loss factors of the cells within the frequency range of 2.5–3.5 kHz. The structures maintain a moderate loss factor over the frequency band of interest with an average value of 0.043 at 3.1 kHz, which is sufficient to achieve high absorption. Since the GIM requires an accurate phase control to induce MIR, which further leads to high absorption, we further compute the bandwidth of individual cells for phase modulation. The reflected phase as a function of the frequency is plotted in Fig. 5(d), where a clear phase difference between adjacent unit cells can be observed. It should be pointed out that MIR will be enforced as long as a linear phase change can be maintained. Although the unit cells are dispersive, the phase gradient is preserved within a bandwidth of around 600 Hz, and therefore the metasurface is expected to have high absorption within this range.

B. Simulation and experiment

To illustrate the effect of loss, we first simulate the metasurface without a loss and compare its reflection by adding a loss factor of 0.043. The corresponding scattered acoustic fields are depicted in Fig. 6. For the case without a loss, the acoustic waves are reflected with an identical x-component wave vector compared to the incident one. When a loss is introduced, the diffracted wave ($m = 0$) is severely suppressed because of the interplay of the loss and MIR. It should be pointed out that a loss factor of 0.043 corresponds to an absorption coefficient of 0.2 for the direct reflection of the unit cell. Clearly, such a low absorption efficiency cannot result in high absorption of the metasurface. Thanks to the MIR process, the retardation for acoustic waves inside the structure is effectively
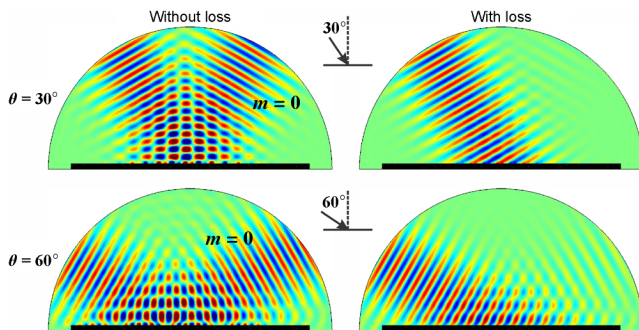

FIG. 6. Simulated acoustic fields for oblique incidence with and without a loss. Top: The incident angle is 30°. Bottom: The incident angle is 60°. Most of the acoustic energy is absorbed when a small amount of loss is introduced.

increased and eventually leads to the high absorption of the $m = 0$ order diffraction.

Numerical simulations and measurements of a 3D-printed prototype are conducted to test the performance of the absorptive metasurface. The sample is printed using acrylonitrile butadiene styrene plastic with density 1230 kg/m^3 and speed of sound 2230 m/s. The walls of the sample are considered to be acoustically rigid, as their impedance is much larger than that of air. The fabricated sample consists of 12 periods, and the overall length, thickness, and height are 67.2, 4.6, and 4.0 cm, respectively, with its thickness about 0.4λ at 3.1 kHz. A portion of the fabricated metasurface is illustrated in Fig. 7(a). The sample is secured in a two-dimensional (2D) waveguide whose height is 4.0 cm to ensure only a zeroth-order wave can propagate inside. A transducer array composed of 28 loudspeakers is used to generate a broadband pulse to the sample. The incident and reflected acoustic signals are recorded simultaneously using a moving microphone within the scan area in front of the sample. The received signals are time gated to extract the incident and reflected wave packets. Inverse Fourier transform is then performed to extract frequency-dependent information. The acoustic pressure field for normal incidence is depicted in Fig. 7(a), which is in good agreement with simulation results. The amplitude of the reflected wave is much smaller than the incident one, as most of the energy is absorbed by the metasurface. The capability of the metasurface is further quantified by measuring and integrating the total scattered energy at 2.7λ away from the sample. The comparison between simulations and experiments is shown in Fig. 7(b) at three discrete frequencies, namely, 2900, 3100, and 3300 Hz. The measurement is performed within an incident angle range from $-40°$ to $40°$, as the size of the waveguide (1.2 m by 1.2 m) is limited and the full reflected wave front cannot be captured at larger angles. The average energy absorption is more than 14 dB at these frequencies, which is consistent with the bandwidth of the individual cells given in Fig. 5(d). The sharp peaks at around $\pm 35°$ is not observed in the measurement due to a fabrication tolerance (e.g., insufficient accuracy of the neck widths). A number of reasons may contribute to the discrepancies between the simulated and measured results. For example, the real loss of the metasurface in the measurement can be dependent on the humidity of air, existence of dust, surface roughness of the 3D-printed samples, etc. The loss factor may also have large variations among the unit cells, which lead to an imperfect collective response of the metasurface. Nevertheless, we emphasize that the high energy absorption clearly demonstrates the wide-angle performance of the metasurface. Figure 7(c) presents the energy-absorption rate of the metasurface as a function of the frequency and incident angle. A peak energy absorption of 20 dB is achieved at a center frequency of around 3.2 kHz in the measurement, which is slightly different from the designed
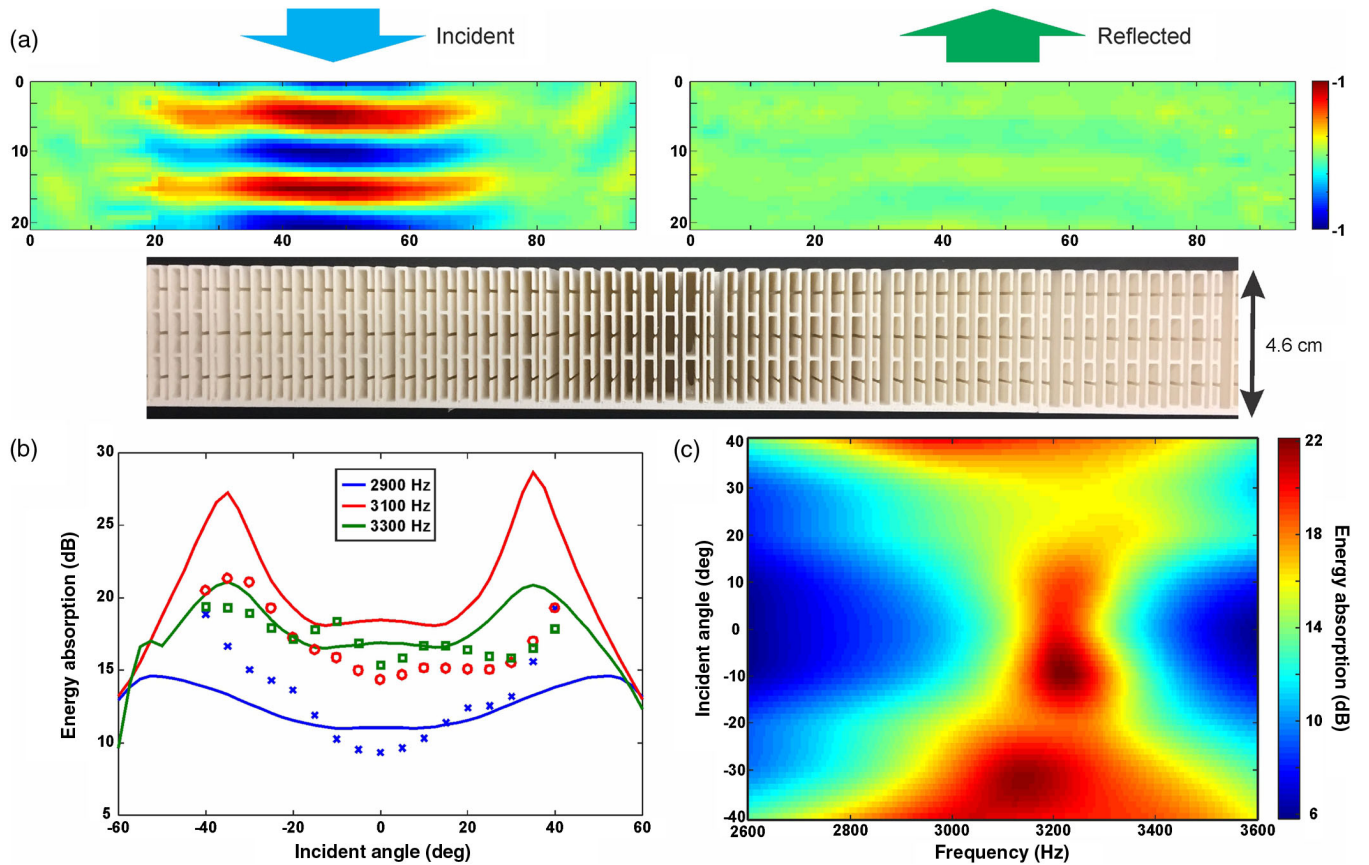
FIG. 7. Performance of the reflective GIM. (a) Measured incident and reflected acoustic fields 30 cm away from the sample. The size of the scan area is 95 cm by 20 cm. The inset shows a portion of the fabricated sample. (b) Simulated and measured energy absorption of the GIM at 2900, 3100, and 3300 Hz. The lines represent numerical results, and the markers denote measured data. (c) Measured absorbing performance of the GIM as a function of the frequency and incident angle. The incident angle range of experimentally obtained energy absorption is −40° to 40°, as part of the reflected beam exceeds the scan area and cannot be captured.

one (3.1 kHz) and may be caused by a fabrication defect. Over 95% energy absorption (corresponds to an absorption rate of over 13 dB) is observed within a frequency band of around 600 Hz, ranging from −40° to 40°. The metasurface also has a moderate absorption coefficient within a wide window of incident angles, which confirms the validity of the design for wide-angle absorption, as MIR is enforced for all angles of incidence. Compared with resonance-based thin sound absorbers such as microperforated plates, the proposed reflective GIM yields a broader bandwidth and better uniformity.

IV. CONCLUSION

In conclusion, we theoretically demonstrate the correlation of diffraction from a reflective GIM and the MIR process inside the unit cells. It is found that MIR plays an important role in the formation of different orders of diffraction when the incident angle is above the critical angle. A highly absorptive metasurface is designed based on the mechanism proposed in the paper. By harnessing the effect of MIR, high absorption is achieved without having

to tailor the individual absorptive response of the unit cells [15,16]. It is shown that a loss factor of as low as 0.043 of the cells is able to absorb most of the incident energy. Since thin acoustic structures, especially acoustic metasurfaces, naturally embrace viscous and thermal losses [31,34], the requirement of a suitable amount of loss can be easily fulfilled. Experiments on a prototype demonstrate the effectiveness of the metasurface. The sound-absorbing scheme proposed here relaxes the necessity of resonance structures which inherently limits the bandwidth and uniformity. To further increase the bandwidth of the metasurface, nondispersive cells may be adopted [27], and the resonance of the Helmholtz resonators in the individual cells may also be considered for the absorption of other frequency contents. The analysis based on MIR can also be readily applied to metasurfaces working on a transmitted scenario for other applications such as asymmetric transmission [21]. The theory can be possibly extended to other classical waves, such as electromagnetic waves to predict the behavior of GIMs working under optical waves. It is hoped that this study could pave the way for the study of MIR and provide an alternative route to design nonresonant sound-absorbing structures.

––––––––––––

[1] L. E. Kinsler, A. U. Frey, A. B. Coppens, and J. V. Sanders, *Fundamentals of Acoustics* (Wiley, New York, 1982).

[2] L. L. Beranek and I. L. Ver, *Noise and Vibration Control Engineering-Principles and Applications* (Wiley, New York, 1992).

[3] D. Maa, Potential of microperforated panel absorber, J. Acoust. Soc. Am. **104**, 2861 (1998).

[4] B.-I. Popa and S. A. Cummer, Non-reciprocal and highly nonlinear active acoustic metamaterials, Nat. Commun. **5**, 3398 (2014).

[5] S. Xiao, G. Ma, Y. Li, Z. Yang, and P. Sheng, Active control of membrane-type acoustic metamaterial by electric field, Appl. Phys. Lett. **106**, 091904 (2015).

[6] Z. Lu, M. Shrestha, and G. K. Lau, Electrically tunable and broader-band sound absorption by using micro-perforated dielectric elastomer actuator, Appl. Phys. Lett. **110**, 182901 (2017).

[7] S. A. Cummer, J. Christensen, and A. Alù, Controlling sound with acoustic metamaterials, Nat. Rev. Mater. **1**, 16001 (2016).

[8] G. Ma and P. Sheng, Acoustic metamaterials: From local resonances to broad horizons, Sci. Adv. **2**, e1501595 (2016).

[9] G. Ma, M. Yang, S. Xiao, Z. Yang, and P. Sheng, Acoustic metasurface with hybrid resonances, Nat. Mater. **13**, 873 (2014).

[10] J. Li, W. Wang, Y. Xie, B. I. Popa, and S. A. Cummer, A sound absorbing metasurface with coupled resonators, Appl. Phys. Lett. **109**, 091908 (2016).

[11] V. Romero-García, G. Theocharis, O. Richoux, A. Merkel, V. Tournat, and V. Pagneux, Perfect and broadband acoustic absorption by critically coupled sub-wavelength resonators, Sci. Rep. **6**, 19519 (2016).

[12] X. Cai, Q. Guo, G. Hu, and J. Yang, Ultrathin low-frequency sound absorbing panels based on coplanar spiral tubes or coplanar Helmholtz resonators, Appl. Phys. Lett. **105**, 121901 (2014).

[13] Y. Li and B. M. Assouar, Acoustic metasurface-based perfect absorber with deep subwavelength thickness, Appl. Phys. Lett. **108**, 063502 (2016).

[14] C. Zhang and X. Hu, Three-Dimensional Single-Port Labyrinthine Acoustic Metamaterial: Perfect Absorption with Large Bandwidth and Tunability, Phys. Rev. Applied **6**, 064025 (2016).

[15] M. Yang, S. Chen, C. Fu, and P. Sheng, Optimal sound-absorbing structures, Mater. Horiz. **4**, 673 (2017).

[16] L. Liu, H. Chang, C. Zhang, and X. Hu, Single-channel labyrinthine metasurfaces as perfect sound absorbers with tunable bandwidth, Appl. Phys. Lett. **111**, 083503 (2017).

[17] V. Leroy, A. Strybulevych, M. Lanoy, F. Lemoult, A. Tourin, and J. H. Page, Superabsorption of acoustic waves with bubble metascreens, Phys. Rev. B **91**, 020301 (2015).

[18] N. Sui, X. Yan, T.-Y. Huang, J. Xu, F.-G. Yuan, and Y. Jing, A lightweight yet sound-proof honeycomb acoustic metamaterial, Appl. Phys. Lett. **106**, 171905 (2015).

[19] T. Huang, C. Shen, and Y. Jing, Membrane- and plate-type acoustic metamaterials, J. Acoust. Soc. Am. **139**, 3240 (2016).

[20] W. Wang, Y. Xie, B. I. Popa, and S. A. Cummer, Subwavelength diffractive acoustics and wavefront manipulation with a reflective acoustic metasurface, J. Appl. Phys. **120**, 195103 (2016).

[21] Y. Li, C. Shen, Y. Xie, J. Li, W. Wang, S. A. Cummer, and Y. Jing, Tunable Asymmetric Transmission via Lossy Acoustic Metasurfaces, Phys. Rev. Lett. **119**, 035501 (2017).

[22] J. Mei and Y. Wu, Controllable transmission and total reflection through an impedance-matched acoustic metasurface, New J. Phys. **16**, 123007 (2014).

[23] C. Shen, Y. Xie, J. Li, S. A. Cummer, and Y. Jing, Acoustic metacages for sound shielding with steady air flow, J. Appl. Phys. **123**, 124501 (2018).

[24] N. Yu, P. Genevet, M. A. Kats, F. Aieta, J.-P. Tetienne, F. Capasso, and Z. Gaburro, Light propagation with phase discontinuities: Generalized laws of reflection and refraction, Science **334**, 333 (2011).

[25] Y. Xie, W. Wang, H. Chen, A. Konneker, B.-I. Popa, and S. A. Cummer, Wavefront modulation and subwavelength diffractive acoustics with an acoustic metasurface, Nat. Commun. **5**, 5553 (2014).

[26] Y. Li, X. Jiang, R. Q. Li, B. Liang, X. Y. Zou, L. L. Yin, and J. C. Cheng, Experimental Realization of Full Control of Reflected Waves with Subwavelength Acoustic Metasurfaces, Phys. Rev. Applied **2**, 064002 (2014).

[27] X. Zhu, K. Li, P. Zhang, J. Zhu, J. Zhang, C. Tian, and S. Liu, Implementation of dispersion-free slow acoustic wave propagation and phase engineering with helical-structured metamaterials, Nat. Commun. **7**, 11731 (2016).

[28] Y. Li, X. Jiang, B. Liang, J. Cheng, and L. Zhang, Metascreen-Based Acoustic Passive Phased Array, Phys. Rev. Applied **4**, 024003 (2015).

[29] Y. Li, S. Qi, and M. B. Assouar, Theory of metascreen-based acoustic passive phased array, New J. Phys. **18**, 043024 (2016).

[30] X. Jiang, Y. Li, and L. Zhang, Thermoviscous effects on sound transmission through a metasurface of hybrid resonances, J. Acoust. Soc. Am. **141**, EL363 (2017).

[31] M. Molerón, M. Serra-garcia, and C. Daraio, Visco-thermal effects in acoustic metamaterials: From total transmission to

total reflection and high absorption, New J. Phys. **18,** 033003 (2016).

[32] N. Jiménez, W. Huang, V. Romero-García, V. Pagneux, and J. P. Groby, Ultra-thin metamaterial for perfect and quasi-omnidirectional sound absorption, Appl. Phys. Lett. **109,** 121902 (2016).

[33] N. Jiménez, V. Romero-García, V. Pagneux, and J. P. Groby, Quasiperfect absorption by subwavelength acoustic panels in transmission using accumulation of resonances due to slow sound, Phys. Rev. B **95,** 014205 (2017).

[34] G. P. Ward, R. K. Lovelock, A. R. J. Murray, A. P. Hibbins, J. R. Sambles, and J. D. Smith, Boundary-Layer Effects on Acoustic Transmission through Narrow Slit Cavities, Phys. Rev. Lett. **115,** 044302 (2015).